

CHANDRA DETECTION OF EJECTA IN THE SMALL-DIAMETER SUPERNOVA REMNANT
G349.7+0.2

J. S. LAZENDIC¹, P. O. SLANE¹, J. P. HUGHES², Y. CHEN³ AND T. M. DAME¹
Draft version February 7, 2020

ABSTRACT

We present high-resolution X-ray observations of the small-diameter supernova remnant (SNR) G349.7+0.2 with the *Chandra X-ray Observatory*. The overall SNR spectrum can be described by two spectral components. The soft component is in ionization equilibrium and has a temperature of ≈ 0.8 keV; the hard spectral component has a temperature of ≈ 1.4 keV, an ionization timescale of $\approx 5 \times 10^{11}$ cm⁻³ s and enhanced abundances of Si. The spatially resolved spectral modeling shows that S may also be enhanced, at least in some regions. The enhanced abundances clearly point to the presence of an ejecta component in this remnant. Using the available H I and CO data towards G349.7+0.2 we derive a column density of $\approx 7 \times 10^{22}$ cm⁻² along the line of sight to the SNR, which is consistent with our X-ray data. The X-ray morphology of G349.7+0.2 is strikingly similar to that at radio wavelengths — an irregular shell with a brighter eastern side — which is consistent with expansion in a medium with a large scale density gradient. The remnant is known to be interacting with a molecular cloud (from the presence of OH(1720 MHz) masers), but this interaction is probably limited to the central portion of the SNR, as seen in SNR IC 443. We found that H I clouds are present in the SNR region, which supports the notion that G349.7+0.2 belongs to a class of remnants evolving in the intercloud medium (such are IC 443 and W44; Chevalier 1999), which is also responsible for the remnant’s morphology. G349.7+0.2 does not have the mixed-morphology found for other maser-emitting SNRs studied to date in X-rays, but its morphology can be explained by a projection model for mixed-morphology SNRs. We have identified a point source close to the center of the SNR with a luminosity of $L_X(0.5 - 10.0 \text{ keV}) \sim (3 - 5) \times 10^{34} d_{22} \text{ ergs s}^{-1}$, which is consistent with that of the compact central objects found in a few other Galactic SNRs.

Subject headings: radiation mechanisms: thermal — supernova remnants — ISM: individual
(G349.7+0.2) — X-rays: ISM

1. INTRODUCTION

G349.7+0.2 is one of the three brightest radio supernova remnants (SNRs) in our Galaxy (Shaver et al. 1985), yet until recently very little was known about it. It is a small diameter remnant ($\approx 2'5$) classified as shell-type with a brighter eastern SNR limb (Shaver et al. 1985). Early H I observations indicated that G349.7+0.2 is located at a distance of 18.3 ± 4.6 kpc (Caswell et al. 1975). OH(1720 MHz) maser emission has been detected towards G349.7+0.2 at a radial velocity of around $+16$ km s⁻¹, implying that the SNR is interacting with dense molecular gas (Frail et al. 1996), and establishing a kinematic distance of 22.4 kpc. The molecular complex associated with the remnant was mapped in the CO 1–0 line (Reynoso & Mangum 2001), while near-infrared and millimeter-line observations have identified the shocked portion of the cloud located towards the center of the remnant (Lazendic et al. 2004). The shocked gas has temperature around 45 K and density around 10^5 cm⁻³, which agrees well with conditions required for OH(1720 MHz) maser production (Lockett, Gauthier & Elitzur 1999).

In the X-ray band G349.7+0.2 was first detected in the *ASCA* Galactic plane survey (Yamauchi et al. 1998). Follow-up pointed observations with *ASCA* showed that the remnant is one of the most luminous SNRs in the X-ray band (Slane et al. 2002), with a thermal spectrum

dominated by strong $K\alpha$ lines from Si, S and Fe. The global spectrum was well fitted by both single equilibrium and nonequilibrium ionization models, with a plasma temperature ≈ 1 keV. The *ASCA* data indicated an age of ~ 2800 yr, an unabsorbed X-ray luminosity of $L_X(0.5 - 10.0 \text{ keV}) \sim 2 \times 10^{37} d_{22} \text{ ergs s}^{-1}$, and an energy release of $\sim 5 \times 10^{50}$ ergs in the supernova explosion. The inferred abundances were consistent with solar values, and the large derived X-ray emitting mass ($\sim 160M_\odot$) showed the gas to be dominated by swept-up interstellar material. These results are consistent with the SNR location near a molecular cloud. However, a detailed morphological assessment and spatially resolved spectral analysis was not possible due to the poor spatial resolution of *ASCA*.

In this paper we present high-resolution X-ray observations of G349.7+0.2 with the *Chandra X-ray Observatory*. We discuss the SNR morphology and plasma properties, compare X-ray data with available atomic and molecular data, and compare the properties of G349.7+0.2 with those of similar SNRs.

2. X-RAY DATA

G349.7+0.2 was observed with the Advanced CCD Imaging Spectrometer (ACIS) on board the *Chandra X-ray Observatory* on 13 May 2002 (ObsID 2785). The SNR was positioned on the ACIS-S3 chip, which has the best

¹ Harvard-Smithsonian Center for Astrophysics, 60 Garden street, Cambridge MA 02138

² Department of Physics and Astronomy, Rutgers, The State University of New Jersey, 136 Frelinghuysen Road, Piscataway, NJ 08854-8019

³ Department of Astronomy, Nanjing University, Nanjing 210093, P. R. China

sensitivity and energy resolution in the soft X-ray bands. Data were taken in full-frame timed-exposure mode with the standard integration time of 3.2 s.

We used the contributed CXC software CORR_TGAIN (Vikhlinin et al. 2003) to correct for time-dependence of the ACIS gain (Grant et al. 2003). After applying the corrections, the overall lightcurve was examined for possible contamination from a time-variable background. After these data reduction processes, the effective exposure was 34 ks from which 48606 photons were observed for the whole remnant.

Data were further reduced using standard threads in the *Chandra* Interactive Analysis of Observations (CIAO) software package v.3.0.2, and Calibration Database (CALDB) v.2.26 which includes the corrected FEF files for the S3 CCD used for making the ACIS response matrices. We used weighted response matrices for spectral fitting to account for CTI effects across the CCD. The low-energy ($E < 1$ keV) quantum efficiency of the ACIS has been degraded by molecular contamination on the optical blocking filter, and correction for this is integrated in the v.3.0.2. CIAO tools for making auxiliary response files.

3. DATA ANALYSIS AND RESULTS

3.1. Spatial Analysis

In Figure 1 we show the exposure-corrected 1.0–8.0 keV band ACIS image of G349.7+0.2. The image has a pixel size of $0''.5$ and was smoothed with a Gaussian filter with a FWHM of $1''$. The emission is dominated by the eastern SNR shell, with the peak emission located to the southeast. The bright region appears complex with several knots of emission. The western SNR shell is weak and diffuse, with no noticeable structure. As shown later, this X-ray morphology is very similar to that in the radio band. The images in different energy bands imply that the emission from the eastern-most part of the SNR shell may be softer with respect to the rest of the SNR.

Five unresolved sources have been detected in the field of G349.7+0.2 using the CELLDETECT procedure in CIAO. Their properties are listed in Table 1, and three sources are marked with circles in Figure 1. Source PS4 (CXOU J171801.0–372617) is the only source located, in projection, within the SNR shell. All the sources have about the same number of counts, except for source PS1. The positions of sources were compared with the US Naval Observatory Guide Star Catalogue⁴ and the 2MASS All-Sky Point Source Catalogue⁵. For sources within $2'$ of the telescope axis, which is true for almost all of the sources (Table 1) the radius (90% confidence) of the *Chandra* position uncertainty is $0''.6$ (see *Chandra* Proposer’s Observatory Guide). Only source 1 has an optical/NIR counterpart (USNO 0525–27848790). The rest of the sources do not have counterparts within $5''$ of their position down to 22 mag in *J* band. Their spectra are hard, so they could be pulsars or background active galactic nuclei. Source 4 is of particular interest since it is located within the SNR and we give it more consideration in the next section.

3.2. Spectral Analysis

The spatially-averaged (global) spectrum from the entire remnant is shown in Figure 2. A background spectrum was extracted from the outer regions of the S3 chip. As observed previously by *ASCA*, the SNR spectrum is dominated by $K\alpha$ line features from Si, S and Fe. In addition, the *Chandra* spectrum shows weaker lines from Mg, Ar and Ca. For spectral fitting we used models for an optically thin thermal plasma that has reached collisional ionization equilibrium (VRAYMOND; Raymond & Smith 1977) and for a plasma that is still being ionized (VPSHOCK; Borkowski, Lyerly, & Reynolds 2001). VPSHOCK is a plane-parallel time-dependent ionizing plasma model for which the ionization timescale, $\tau = n_e t$, describes the progress of the plasma towards equilibrium and can assume a range of values between the specified lower (usually set to zero) and upper limits. Since the version v.1.1 of the VPSHOCK model we used for the spectral fitting does not include the Ar line, we added a narrow Gaussian component at ≈ 3.1 keV in our fits.

Single-component VRAYMOND or VPSHOCK models with solar abundances, acceptable for analysis of the overall *ASCA* spectrum from G349.7+0.2, were not able to give a satisfactory fit to the overall *Chandra* spectrum. A good fit was obtained using a VPSHOCK model with enhanced Si abundance, and is significantly improved by adding an equilibrium thermal component with solar abundances; the best-fit parameters are listed in Table 2. This result implies that the plasma in G349.7+0.2 is comprised of multiple components, with a softer component having plasma temperature around 0.8 keV, and a harder component having plasma temperature around 1.4 keV. We show the contribution of both components to the global spectrum in Figure 2. As expected, the harder component (dashed line) dominates the spectrum above 3 keV, while the softer component (dotted line) dominates below that. We find no strong nonthermal emission in G349.7+0.2 and estimate the power law component contribution to the observed flux from the whole SNR region to be less than 2.6% for photon index values between 1.5 and 3 at the 3σ confidence level.

The Si abundance in G349.7+0.2 is clearly enhanced; the χ^2 value of the VPSHOCK+VRAY model drops by 46 when one additional free parameter (the Si abundance) is added. Additional elemental abundances were thawed one by one based on the inspection of the residuals, but only the additional Si in the VPSHOCK (hard) component improved the fit significantly. This enhanced Si abundance implies that we have detected for the first time a SN ejecta component in this SNR. This also implies that the soft spectral component, which has solar abundances, is most likely related to the forward shock, i.e., shocked interstellar material. The ionization timescales obtained for the two components are consistent with this scenario. The forward shock is encountering interstellar material that is denser than that of the SNR interior, and will therefore reach ionization equilibrium faster than shocked ejecta that is expanding in the rarefied SNR interior. The hydrogen column density obtained from the global *Chandra* spectrum is consistent with that obtained from the *ASCA* data (Slane et al. 2002). Such a large column density confirms

⁴ Available at <http://cdcdwww.dao.nrc.ca/usno/>

⁵ Available at <http://irsa.ipac.caltech.edu/>

a considerable absorption of the soft emission from the SNR and is consistent with its relative distance. The X-ray luminosity derived from the global SNR spectrum is $L_X(0.5 - 10.0 \text{ keV}) \approx 3.7 \times 10^{37} d_{22} \text{ ergs s}^{-1}$. We note that the value obtained for the plasma temperature from the global *ASCA* spectrum represents an intermediate value between the two temperatures detected with *Chandra*.

The spectra from the whole SNR can therefore be fitted with two plasma components. Could these two components be separate parts of a single evolving shock? To test this we also fitted the spectral regions with a single planar, initially unequilibrated shock (from Rakowski, Ghavamian, & Hughes 2003). In this model the temperatures of the electrons and protons equilibrate downstream through Coulomb collisions, providing a natural range in temperatures and ionization timescales behind the shock. However, even in this model the best-fit ionization timescales of the Si and S lines differ significantly such that no single component model can accurately fit both line complexes at once.

The high spatial resolution of the *Chandra* data allow us to perform a spatially resolved spectral analysis of G349.7+0.2 to search for spectral variations across the SNR. We selected 6 extraction regions, shown in Figure 1, positioned along the SNR brightness gradient and each containing around 5000 counts. Spectra were re-grouped to include at least 25 counts per bin. As for the global SNR spectrum, the spectrum used for background subtraction was extracted from the outer regions of the S3 chip.

Unlike the overall SNR spectrum, spectra from the individual SNR regions can be well fitted with single-component thermal models whose parameters vary from region to region; the fit parameters are listed in Table 3 and the spectra are shown in Figure 3. All the regions, except the eastern-most region (region 1), favor the VP-SHOCK model over the VRAYMOND model; this implies that most of the plasma in G349.7+0.2 has not yet reached ionization equilibrium and is still evolving. Furthermore, all the regions except the eastern-most region prefer the presence of enhanced Si. Similarly, only the western-most region (region 6) prefers, in addition to Si, an enhanced abundance of S. For completeness, in Table 3 we list the values of Si and S abundances for all the regions. Plasma temperatures, ionization timescales and column densities measured from the individual regions and the global SNR spectrum are plotted in Figure 4. The temperatures derived from individual regions have values intermediate to those of the soft and hard spectral components derived from the global spectrum. This suggests that the individual regions do not have sufficient statistics to distinguish between the two plasma components detected in the global SNR spectrum, and represent an average of the two components summed along the line of sight. The two eastern regions, regions 1 and 2, appear to have a lower plasma temperature than the other regions, suggesting that the softer component dominates in the eastern SNR region. Similarly, the fact that these two regions do not show the presence of Fe-K line emission like the other regions suggests that plasma temperature in these two regions is lower than elsewhere in the remnant. Figure 4 also implies that there may be a small variation in ionization timescale and column density across the SNR (e.g., regions 1, 2 and 3

versus regions 4 and 6).

To investigate the spatial distribution of Si and S line emission across the remnant on a finer scale than that of the spectral extraction regions, we produced continuum-subtracted (CS) and equivalent-width (EW) images (see e.g., Park et al. 2003), shown in Figure 5. Narrow-band images used for deriving the CS and EW images were filtered in energy according to Table 4, and binned by $8''$ to provide a sufficient number of counts in the faint SNR regions. We found that the CS images for Si and S are quite similar to the whole band image. The EW images, which represent line strength compared to the continuum, do not show any spatial variation for the Si and S lines, which appears inconsistent with the results obtained from spectral modeling, at least for S. However, the EW of the emission lines does not depend just on the total number of emitting atoms that are present in the plasma, but also on the temperature and ionization state of the plasma. Region 6, where an enhanced abundance of S is derived from the spectral fit, is the same region where the ionization timescale is low, which also makes the line-to-continuum ratio lower than expected for an equilibrium plasma. The net result is that the S EW is relatively uniform across the remnant. This is confirmed by measuring EWs directly from spectra of the two representative SNR regions. The derived EWs for the Si(S) line in regions 2 and 6 are $0.40 \pm 0.03(0.24 \pm 0.02) \text{ keV}$ and $0.36 \pm 0.03(0.28 \pm 0.02) \text{ keV}$, respectively.

3.3. SNR parameters

To derive mean electron density n for the two plasma components, we approximate the X-ray emitting volume V as a sphere 6.4 pc in radius, and denote f_s and f_h as filling factors for the soft and hard emission components, respectively. The emission measure for each component ($i = h, s$) is $EM_i \approx (n_i^2 f_i V)/(4\pi d^2)$. Assuming that the soft and hard thermal components are roughly in pressure equilibrium ($n_s T_s \approx n_h T_h$), we can derive their relative filling factors: $f_h/f_s = (EM_h/EM_s)/(n_h/n_s)^2 = (EM_h/EM_s)/(T_s/T_h)^2$. Here we assume that the plasma temperature we measure represents the temperature of all species (electrons and ions), although the X-ray fits only provide the electron temperature. Substituting in the fitted values from Table 2, we find that $f_h/f_s \approx 1.05$. However, in the case that the whole SNR volume is not emitting X-rays, we set $f_V = f_s \approx f_h$ to account for the unknown volume filling factor. The electron densities are then $n_s \gtrsim 5.0 f_V^{-1/2} d_{22}^{-1/2} \text{ cm}^{-3}$ and $n_h \gtrsim 2.7 f_V^{-1/2} d_{22}^{-1/2} \text{ cm}^{-3}$. The X-ray emitting mass can be found from $M_x = 1.4 n_H m_H f_V V$, which gives $M_s \lesssim 136 f_V M_\odot$ mass in the soft component and $M_h \lesssim 40 f_V M_\odot$ mass in the hard component.

Hnatyk & Petruk (1999) showed that the global characteristics of a SNR expanding into a density gradient will be similar to those of the Sedov (adiabatic) SNR, because there is a mutual compensation of the emission deficit from the low density regions by the enhanced emission from the high density regions. The shock temperature is thus related to the plasma temperature as in the Sedov (1959) model: $T_{sh} = 0.78 T_X \approx 7 \times 10^6 \text{ K}$, for $kT_X \approx 0.76 \text{ keV}$ (using the temperature of the soft spectral component which is most probably the forward shock component, as

suggested previously). The corresponding shock velocity can be calculated from $v_{sh} = (16kT_{sh}/3\mu m_H)^{1/2} \approx 710 \text{ km s}^{-1}$, where $\mu = 0.604$ is the mean atomic weight. The SNR age is proportional to the shock radius and velocity, $t = 2r_{sh}/5v_{sh}$. We adopt the SNR radius of $1'$, for which its dimensional size is $r \approx 6.4 d_{22} \text{ pc}$, and derive an SNR age of $t \approx 3500 d_{22} \text{ yr}$. This is in agreement with the upper limits derived from the ionization timescales of the two components of $t \leq 4500 \text{ yr}$. The explosion energy is approximately $E = 4.6 \times 10^{-25} (n_s/4) (r_{sh}^5/t^2) \sim 1.3 \times 10^{50} f_V^{1/2} d_{22}^{5/2} \text{ ergs}$, using the value of n_s derived above. This is a slightly lower energy than the canonical value of 10^{51} ergs , although the uncertainty on the density n_s could modify this estimate somewhat.

3.4. Point Source

The X-ray emission from the point source CXOU J171801.0–372617 found inside the SNR shell is hard (Table 1), and there is a possibility that this source is a neutron star associated with the SNR. Indeed, in our *ASCA* study we suggested that G349.7+0.2 could be the remnant of a core-collapsed supernova (Slane et al. 2002). Because the total number of counts from the point source is too low for spectral analysis, we estimated the unabsorbed flux using the count rate ($\approx 9.4 \times 10^{-3} \text{ counts s}^{-1}$), the effective area and response matrix files for ACIS-S. Neutron stars are found with a range of photon index values, with classical young pulsars having values between 1.1–1.7 (e.g. Chakrabarty et al. 2001) and more exotic objects like compact central objects (CCOs) and anomalous X-ray pulsars (AXPs) having a softer photon index of ~ 4 and a blackbody component with temperature between 0.2–0.4 keV (Pavlov et al. 2002; Pavlov 2003). Thus, assuming the same column density as for the SNR ($7 \times 10^{22} \text{ cm}^{-2}$) and a power law photon index between 1.1 and 4.0 we obtained an unabsorbed integrated flux in the 0.5–10.0 keV range of $F_X^0 \sim (5-8) \times 10^{-13} \text{ ergs cm}^{-2} \text{ s}^{-1}$, which at a distance of 22 kpc gives an X-ray luminosity of $L_X \sim (3-5) \times 10^{34} \text{ ergs s}^{-1}$. This luminosity is lower than the values found from the other young pulsars, and is closer to the luminosities found from CCOs, such as the one in SNR G347.3–0.5 (Lazendic et al. 2003). There is no obvious compact source at the location of our point source in the radio image, but some diffuse emission is present at the 15 mJy beam^{-1} level. Using the number of sources as a function of flux density from the *Chandra* Multi-wavelength Plane Survey (Grindlay et al. 2003), we derive a chance probability of ≈ 0.2 for finding an unrelated source with the X-ray brightness of $\sim 10^{13} \text{ ergs cm}^{-2} \text{ s}^{-1}$ (assuming a power law photon index of 1.7) within the boundary of the SNR. Thus, the X-ray luminosity, and lack of an optical and radio counterpart at the present sensitivity of the observations is consistent with a possibility that point source in G349.7+0.2 is an associated CCO.

4. COLUMN DENSITY TOWARDS THE SNR

We also examined 21-cm HI emission towards the G349.7+0.2 region from the Southern Galactic Plane Survey (SGPS) data with angular resolution of $\approx 2'.5$ (e.g., McClure-Griffiths et al. 2001). The 21 cm spectrum toward the remnant shows very strong absorption at all negative velocities ($R < R_C$) and at positive velocities up to

+8 km s^{-1} . This places the SNR slightly beyond the solar circle on the far side. Adopting the molecular cloud velocity of +16 km s^{-1} and using a flat rotation curve beyond the solar circle, the kinematic distance is 23.0 kpc, as found by Frail et al. (1996).

The Galactic center CO survey of (Bitran et al. 1997) covers this region with beamwidth ($1/8^\circ$) sampling. Integrating the nearest CO spectrum over the range $v = -220$ to +17 km s^{-1} and using the CO-to-mass conversion factor $X = 1.8 \times 10^{20} \text{ cm}^{-2} \text{ K}^{-1} \text{ km s}^{-1}$ (Dame, Hartmann, & Thaddeus 2001) we obtain:

$$2 \times N(\text{H}_2) = 4.6 \times 10^{22} \text{ atoms cm}^{-2}.$$

The 21 cm velocity-integrated intensity varies very smoothly in longitude and latitude through the position of the remnant, and to obtain the atomic column density we used the average 21 cm spectrum over a small rectangle ($27' \times 21'$) surrounding the remnant, but excluding a smaller region ($15' \times 9'$) of absorption directly toward the remnant. A lower limit on the atomic column density can be obtained by assuming the 21 cm emission is optically thin. This yields:

$$N(\text{HI}) > 1.5 \times 10^{22} \text{ cm}^{-2}.$$

Adopting a standard HI spin temperature of 140 K yields an atomic column density of

$$N(\text{HI}) = 2.8 \times 10^{22} \text{ cm}^{-2}.$$

Therefore:

$$N(\text{total}) = N(\text{HI}) + 2 \times N(\text{H}_2) = 7.3 \times 10^{22} \text{ cm}^{-2},$$

which agrees well with the value derived from X-ray observations.

5. DISCUSSION

5.1. SNR Morphology and Interaction with Ambient Medium

The X-ray morphology of G349.7+0.2 revealed with the *Chandra* observations is strikingly similar to that of the radio image (Lazendic et al. 2004), shown as contours in Figure 6. Previous studies in the radio band have suggested that the structure of G349.7+0.2 is consistent with two overlapping rings, with the fainter, larger ring corresponding to the side where the SNR shock is encountering a lower-density medium (Manchester 1987; Reynoso & Mangum 2001). This interpretation is consistent with theoretical modeling of SNR expansion in a medium with a density gradient (e.g., Tenorio-Tagle, Bodenheimer, & Yorke 1985). Since the SNR shock moves slowly in the dense cloud and faster in the lower density medium, two half shells with different radii are expected to be seen, with the shell radii depending on the initial location of the explosion and the steepness of the density gradient. In addition, Hnatyk & Petruk (1999) performed 2-D hydrodynamical modeling of the evolution and X-ray emission of SNRs expanding in a large-scale density gradient, as seen by an observer under different viewing angles. Compared to their model, the morphology of G349.7+0.2 is broadly consistent with a large scale density gradient seen by an observer at an angle of $\approx 45^\circ$.

G349.7+0.2 shows some morphological resemblance to another Galactic SNR associated with OH(1720 MHz)

masers, IC 443. The two remnants are of similar age and spatial size, and radio and X-ray morphology of IC 443 is also consistent with expansion into a large scale density gradient (Hnatyk & Petruk 1998) produced by an H I cloud on the east and south-east side of the SNR (e.g., Braun & Strom 1986). In IC 443, an interaction with a CO cloud is occurring in the central region, where shocked molecular gas and OH(1720 MHz) maser emission is found (e.g., Burton et al. 1988; van Dishoeck, Jansen, & Phillips 1993; Claussen et al. 1997). In Figure 7a we show the distribution of the molecular cloud associated with G349.7+0.2, as traced by the CO 1–0 emission (Reynoso & Mangum 2001), superimposed on the *Chandra* image. The molecular cloud interaction with G349.7+0.2 also appears to be limited to the central part of the remnant. The location of OH(1720 MHz) masers (Frail et al. 1996), also shown in Figure 7a, point to the on-going interaction between the CO cloud and the SNR. OH masers originate from shocked molecular clumps with density around 10^5 cm^{-3} and temperature of 50–125 K, which have encountered the shock propagating transverse to the line of sight (Elitzur 1976; Lockett, Gauthier & Elitzur 1999). Shocked H_2 2.12 μm emission has also been detected at the locations of the OH masers (Lazendic et al. 2004). The velocity-integrated H_2 1–0 S(1) emission is shown in Figure 7b, superimposed on the *Chandra* image. The H_2 line emission originates from the warm ($\sim 10^3 \text{ K}$) gas just behind the part of the shock front expanding into the molecular cloud. The H_2 emission is also situated in the center of the SNR where X-ray emission is very faint. It is possible that due to high density in this region the SNR shock became radiative and we see the transmitted shock through the molecular cloud, that radiates mostly in IR band; mid-IR and far-IR emission has also been detected from this part of the SNR (Lazendic et al. 2004). Thus, the density gradient responsible for the morphology of G349.7+0.2 is probably produced by H I clouds, as seen in IC 443. Velocity-integrated (+14 to +20 km s^{-1}) H I emission is shown in Figure 8 overlaid with contours of CO integrated over the same velocity range and the 18 cm radio image of the SNR. The overall large scale morphology of the atomic gas is consistent with that of the molecular gas. The H I gas follows the distribution of the large CO shell, with H I emission peaks not always coinciding with the CO peaks, as is commonly found between atomic and molecular gas. Thus, H I material is present in the region towards G349.7+0.2.

The density, size, and luminosity of G349.7+0.2 are similar to those proposed by Chevalier (1999) for Galactic SNRs expanding into an intercloud medium, and to those of compact SNRs in other galaxies (Chevalier & Fransson 2001). These remnants are expanding into molecular clouds, but because of the clumpy structure of molecular clouds and the small filling factor of dense clumps, the remnant is mostly expanding into an intercloud medium with densities 5–25 cm^{-3} (Chevalier 1999). Indeed, the molecular cloud associated with G349.7+0.2 has a density of $\sim 10^3 \text{ cm}^{-3}$, whereas densities determined from X-ray emitting plasma of $\sim 5 \text{ cm}^{-3}$ are more characteristics of an intercloud H I medium. This high density of ambient medium results in a rapid SNR evolution and a large amount of swept-up material producing very high luminosity ($\sim 10^{37} \text{ erg s}^{-1}$) in a short period just before the

SNR becomes radiative and starts to cool rapidly. Such remnants can be recognized by a high radio surface brightness (e.g., IC 443 and W44; Chevalier 1999) or a strong IR flux (Chevalier & Fransson 2001). The X-ray observations of G349.7+0.2 imply that this SNR is still dynamically young enough to produce a significant X-ray flux, in addition to strong radio flux. The radiative part of the shell should be accompanied by a H I shell. However, high-resolution observations towards G349.7+0.2 are needed to investigate the association between the H I emission and the SNR shock.

5.2. Detection of Ejecta and the Two-Component SNR Plasma

The solar abundances and large X-ray emitting mass derived from *ASCA* observations imply that the X-ray emitting gas in G349.7+0.2 is dominated by swept-up interstellar material (Slane et al. 2002). The implication is that, similar to the case of the SNR N132D in the Large Magellanic Cloud (e.g. Hughes 1987), the SN ejecta component, expected from such a young SNR, is largely hidden by the glow of massive amounts of swept-up material. In the case of N132D, optical studies showed clear evidence of fast-moving ejecta synthesized in the collapse of a massive star. In X-rays, there was initially no detection of ejecta, but high resolution spectral studies indicated enhanced levels of oxygen (Hwang et al. 1993), and the presence of an additional higher temperature spectral component which could be related to the ejecta (Favata et al. 1997; Behar et al. 2001). With the *Chandra* observations, we clearly detect enhanced abundances of Si and possibly of S in G349.7+0.2, which provides the first evidence for the presence of ejecta in this remnant. Similar evidence for the presence of ejecta in two middle-aged Large Magellanic Cloud SNRs, 0548–70.4 and 0534–69.9, with substantial amount of swept-up material ($\sim 50 M_{\odot}$) has been presented by Hendrick, Borkowski, & Reynolds (2003), who derive enhanced Fe abundance based on the *Chandra* spectra of these remnants.

The detection of the enhanced abundances only in the harder spectral component suggests that this component is associated with the SN ejecta, which means that the softer spectral component is related to the forward shock and the swept-up material. If the ambient medium into which the SNR is expanding has much lower density than that of the ejecta, the forward shock will be heated to a significantly higher temperature than the ejecta; this is the case in the young SNR Cas A (e.g., Willingale et al. 2002). However, G349.7+0.2 is expanding into a dense medium and it is possible that the forward shock is cooler than the ejecta. The assumed density gradient in the ambient medium could yield enhanced S in just the western-most region, as hinted at in the data; the amount of swept-up material is lowest there because of the low ambient density, which enables the ejecta component to have a larger filling factor relative to the eastern regions where the ambient density is higher. Indeed, the fits to all the other regions (1 through 5) could accommodate a contribution from the plasma component of region 6 with an emission measure an order of magnitude lower than the components listed in Table 3.

The lower limit on the fractional mass of ejecta can be

inferred from $M_{ejecta}/M_{total} \geq (a - 1) * M_{solar}/M_{total}$, where a is the measured abundance, and M_{solar}/M_{total} is the standard solar mass fraction; for Si and S the mass fractions are 6.96×10^{-4} and 4.79×10^{-4} , respectively (Grevesse & Sauval 1998). Using the measured abundances from region 6, we derive $M_{Si}/M_{total} \geq 9.74 \times 10^{-4}$ and $M_S/M_{total} \geq 2.39 \times 10^{-4}$. The observed emission measure in region 6 implies a gas density of $n_H \approx 2.3 \text{ cm}^{-3}$, which for an emission volume of $\approx 1.4 \times 10^{58} \text{ cm}^3$ ($32'' \times 113'' \times 144''$) gives a total mass in the region of $\approx 34 f_V M_\odot$. The mass of the observed Si and S ejecta is thus $\geq 0.033 f_V M_\odot$ and $\geq 0.008 f_V M_\odot$, respectively. This is a significant fraction of the amount produced by 13–15 M_\odot stars (Si: $0.047\text{--}0.07 M_\odot$, S: $0.026\text{--}0.023 M_\odot$; Thielemann, Nomoto, & Hashimoto 1996).

5.3. Implications for Mixed-Morphology SNRs

OH(1720 MHz) maser emission such as that associated with G349.7+0.2 and IC 443, has been found in about 10% of the Galactic SNRs (e.g. Green et al. 1997; Wardle & Yusef-Zadeh 2002). Seven of these maser-emitting (ME; Yusef-Zadeh et al. 2003) SNRs have been studied in detail in X-rays, and all of them are found to be of the mixed-morphology (MM; Rho & Petre 1998) class of SNRs. MM remnants, also known as thermal composites, are identified by shell emission in the radio band, and centrally brightened thermal emission in the X-ray band with little or no shell brightening. The evolutionary characteristics which lead to mixed-morphology X-ray properties in SNRs are not well understood, and different models have been suggested to explain individual cases. One such model invokes evaporation of clouds which are left relatively intact after the passage of the SNR blast wave and are evaporating in the SNR interior (White & Long 1991). Another model explains the emission for the mixed morphology SNR W44 (Cox et al. 1999) as due to the effect of thermal conduction in the remnant interior. Another model for mixed morphology SNRs invokes shell-like SNR evolution at the edge of a molecular cloud, in which the ambient density gradient does not lie in the projection plane (Petruk 2001).

A possible correlation between ME and MM SNRs has been suggested, because both types of SNRs appear to be associated with molecular clouds (Green et al. 1997; Rho & Petre 1998). The fact that some MM SNRs do not have OH masers is not unexpected because very specific physical conditions are required for the maser excitation. However, it has been suggested that all ME SNRs could be of the MM class (Rho & Petre 1998; Yusef-Zadeh et al. 2003). G349.7+0.2 is then an example of a ME SNR which does not exhibit MM morphology. Its morphology, which is not centrally peaked, can be explained by the projection effect model used to explain MM SNRs as well (Petruk 2001). As shown in previous sections, we are likely seeing the SNR expanding into a density gradient of an angle of $\approx 45^\circ$. If we were to observe the expansion along the direction of the density gradient, we would see centrally peaked X-ray emission rather than two overlapping shells. Another example is the only ME SNR in the Large Magellanic Cloud, N49 (Brogan et al. 2004). This remnant also has an irregular shell morphology in both radio and X-rays, with a bright region to the south-east (e.g., Park et al. 2003), which can similarly be explained as result-

ing from expansion in a density gradient produced by the presence of a molecular cloud, as mapped by Banas et al. (1997). Thus, if ME and MM SNRs are the same class of the SNRs and there is a single mechanism to explain their appearance and spectral characteristics, the observations of G349.7+0.2 would support the projection model. Identifying more cases of SNRs expanding into density gradients seen under different angles might provide further support for the projection model and contribute towards understanding the nature of MM SNRs.

6. CONCLUSIONS

We present high-resolution *Chandra* observations of a small-diameter SNR, G349.7+0.2. Its X-ray morphology is almost identical to that at radio wavelengths, and is consistent with expansion into a density gradient viewed at an angle of $\approx 45^\circ$. We investigated the atomic and molecular material in the vicinity of the SNR, and suggest that the SNR belongs to the class of SNRs expanding into an intercloud medium discussed by Chevalier (1999). The interaction with the molecular cloud is probably limited to the central portion of the SNR, where the SNR shock became radiative and the shocked material radiates mostly in the IR band (Lazendic et al. 2004). G349.7+0.2 belongs to a class of maser-emitting SNRs which have been suggested to be related to the mixed-morphology class of SNRs. G349.7+0.2 does not exhibit mixed-morphology, but its brightness distribution can be explained with the projection model for mixed-morphology SNRs.

The spectrum from the whole SNR can be fitted with two thermal components, produced by distinct swept-up and ejecta plasma contribution. The softer component has a plasma temperature $\approx 0.8 \text{ keV}$ and is in ionization equilibrium, while the harder component has plasma temperature $\approx 1.4 \text{ keV}$, ionization timescale $\approx 4 \times 10^{11} \text{ cm}^{-3} \text{ s}$ and enhanced abundances of Si. The slightly enhanced S in just the western-most part of the SNR could, if correct, be explained by a higher filling factor of the ejecta component relative to the swept-up component because of the lower density of the ambient medium in that region. The column density to the SNR of $\approx 7 \times 10^{21} \text{ cm}^{-2}$ derived from X-ray data agrees well with the value derived from HI and CO data.

We find a point source with a small number of counts (≈ 30) close, in projection, to the SNR center. Using the column density value found towards the SNR and the observed range of photon index values from neutron stars, we estimate the luminosity of the point source in the 0.5–10.0 keV band to be $\sim (3 - 5) \times 10^{34} d_{22} \text{ erg s}^{-1}$. This luminosity and the lack of an optical and radio counterpart suggests that the X-ray point source could be the compact object formed by the explosion that also produced in G349.7+0.2.

We thank Cara Rakowski for use of her shock model, John Raymond, Oleh Petruk and Sangwook Park for helpful discussions, Estela Reynoso for the CO image and Bryan Gaensler for the HI data. This work was supported in part from *Chandra* grants GO2-3080A (JSL) and GO2-3080B (JPH), and NASA contract NAS 8-39073 (POS).

REFERENCES

- Banas, K. R., Hughes, J. P., Bronfman, L., & Nyman, L.-A. 1997, *ApJ*, 480, 607
- Behar, E., Rasmussen, A. P., Griffiths, R. G., Dennerl, K., Audard, M., Aschenbach, B., & Brinkman, A. C. 2001, *A&A*, 365, L242
- Bitran, M., Alvarez, H., Bronfman, L., May, J., & Thaddeus, P. 1997, *A&AS*, 125, 99
- Borkowski, K. J., Lyerly, W. J., & Reynolds, S. P. 2001, *ApJ*, 548, 820
- Braun, R. & Strom, R. G. 1986, *A&AS*, 63, 345
- Brogan, C. L., Frail, D. A., Goss, W. M., & Troland, T. H. 2000, *ApJ*, 537, 875
- Brogan, C. L., Goss, W. M., Lazendic, J., & Green, A. J. 2004, accepted in *AJ* (astro-ph/0405378)
- Bronfman, L., Nyman, L., & May, J. 1996, *A&AS*, 115, 81
- Burton, M. G., Geballe, T. R., Brand, P. W. J. L. & Webster, A. S. 1988, *MNRAS*, 231, 617
- Caswell, J. L., Murray, J. D., Roger, R. S., Cole, D. J., & Cooke, D. J. 1975, *A&A*, 45, 239
- Chakrabarty, D., Pivovarov, M. J., Hernquist, L. E., Heyl, J. S., & Narayan, R. 2001, *ApJ*, 548, 800
- Chevalier, R. A. 1999, *ApJ*, 511, 798
- Chevalier, R. A. & Fransson, C. 2001, *ApJ*, 558, L27
- Cox, D. P., Shelton, R. L., Maciejewski, W., Smith, R. K., Plewa, T., Pawl, A., & Różycka, M. 1999, *ApJ*, 524, 179
- Claussen, M. J., Frail, D. A., Goss, W. M. & Gaume, R. A. 1997, *ApJ*, 489, 143
- Dame, T. M., Hartmann, D., & Thaddeus, P. 2001, *ApJ*, 547, 792
- Elitzur, M. 1976, *ApJ*, 203, 124
- Favata, F., Vink, J., Parmar, A. N., Kaastra, J. S., & Mineo, T. 1997, *A&A*, 324, L45
- Frail, D. A., Goss, W. M., Reynoso, E. M., Giacani, E. B., Green, A. J. & Otrupcek, R. 1996, *AJ*, 111, 1651
- Grant, C. E., Prigozhin, G. Y., LaMarr, B., & Bautz, M. W. 2003, *Proc. SPIE*, 4851, 140
- Green, A. J., Frail, D. A., Goss, W. M. & Otrupcek, R. 1997, *AJ*, 114, 2058
- Grevesse, N. & Sauval, A. J. 1998, *Space Science Reviews*, 85, 161
- Grindlay, J., et al. 2003, *Astronomische Nachrichten*, 324, 57
- Hendrick, S. P., Borkowski, K. J., & Reynolds, S. P. 2003, *ApJ*, 593, 370
- Hnatyk, B. & Petruk, O. 1998, *Cambridge Monographs in Physics*, 1, 655
- Hnatyk, B. & Petruk, O. 1999, *A&A*, 344, 295
- Hughes, J. P. 1987, *ApJ*, 314, 103
- Hwang, U., Hughes, J. P., Canizares, C. R., & Markert, T. H. 1993, *ApJ*, 414, 219
- Lazendic, J. S., Slane, P. O., Gaensler, B. M., Plucinsky, P. P., Hughes, J. P., Galloway, D. K., & Crawford, F. 2003, *ApJ*, 593, L27
- Lazendic, J. S., Wardle, M., Green, A. J., Whiteoak, J. B., Burton, M. G. 2004, submitted to *MNRAS* (astro-ph/0409302)
- Lockett, P., Gauthier, E. & Elitzur, M. 1999, *ApJ*, 511, 235
- Manchester, R. N. 1987, *A&A*, 171, 205
- McClure-Griffiths, N. M., Green, A. J., Dickey, J. M., Gaensler, B. M., Haynes, R. F., & Wieringa, M. H. 2001, *ApJ*, 551, 394
- Park, S., Burrows, D. N., Garmire, G. P., Nousek, J. A., Hughes, J. P., & Williams, R. M. 2003, *ApJ*, 586, 210
- Pavlov, G. G., Sanwal, D., Garmire, G. P., & Zavlin, V. E. 2002, *ASP Conf. Ser.* 271: Neutron Stars in Supernova Remnants, eds. P. O. Slane & B. M. Gaensler, 247
- Pavlov, G. G. 2003, *IAU Symposium No.* 218
- Petre, R., Szymkowiak, A. E., Seward, F. D., & Willingale, R. 1988, *ApJ*, 335, 215
- Petruk, O. 1999, *A&A*, 346, 961
- Petruk, O. 2001, *A&A*, 371, 267
- Rakowski, C. E., Ghavamian, P., & Hughes, J. P. 2003, *ApJ*, 590, 846
- Raymond, J. C. & Smith, B. W. 1977, *ApJS*, 35, 419
- Reynoso, E. M. & Mangum, J. G. 2001, *AJ*, 121, 347
- Rho, J. & Petre, R. 1998, *ApJ*, 503, L167
- Sedov, L. I. 1959, *Similarity and Dimensional Methods in Mechanics*, New York: Academic Press, 1959
- Shaver, P. A., Salter, C. J., Patnaik, A. R., van Gorkom, J. H., & Hunt, G. C. 1985, *Nature*, 313, 113
- Slane, P., Chen, Y., Lazendic, J. S., & Hughes, J. P. 2002, *ApJ*, 580, 904
- Tenorio-Tagle, G., Bodenheimer, P., & Yorke, H. W. 1985, *A&A*, 145, 70
- Thielemann, F., Nomoto, K., & Hashimoto, M. 1996, *ApJ*, 460, 408
- Townsley, L. K., Broos, P. S., Garmire, G. P., & Nousek, J. A. 2000, *ApJ*, 534, L139
- van Dishoeck, E. F., Jansen, D. J., & Phillips, T. G. 1993, *A&A*, 279, 541
- Vikhlinin, A., Schulz, N., Tibbetts, K., & Edgar, R. 2003, *Chandra* calibration memo (available at <http://cxc.harvard.edu/contrib/alexey/tgain/tgain.html>)
- Wardle, M. & Yusef-Zadeh, F. 2002, *Science*, 296, 2350
- White, R. L. & Long, K. S. 1991, *ApJ*, 373, 543
- Willingale, R., Bleeker, J. A. M., van der Heyden, K. J., Kaastra, J. S., & Vink, J. 2002, *A&A*, 381, 1039
- Yamauchi, S., Koyama, K., Kinugasa, K., Torii, K., Nishiuchi, M., Kosuga, T., & Kamata, Y. 1998, *Astronomische Nachrichten*, 319, 111
- Yusef-Zadeh, F., Wardle, M., Rho, J., & Sakano, M. 2003, *ApJ*, 585, 319

TABLE 1
PROPERTIES OF SERENDIPITOUS SOURCES IN THE FIELD OF G349.7+0.2.

Source	Name	R.A.	Decl.	ACIS counts	Pointing offset	Hardness ratio ^a	Optical/IR counterpart
1	CXOU J171816.2-372556	17 18 16.19	-37 25 55.84	72 ± 9	2'3	-0.6 ± 0.5	yes, $J(\text{mag})=10$
2	CXOU J171807.3-372707	17 18 07.32	-37 27 07.66	30 ± 6	1'5	0.10 ± 0.10	no
3	CXOU J171805.7-372437	17 18 05.67	-37 24 37.41	26 ± 5	1'2	0.86 ± 1.19	no
4	CXOU J171801.0-372617	17 18 01.00	-37 26 16.62	32 ± 6	0'8	0.35 ± 0.34	no
5	CXOU J171746.1-372506	17 17 46.10	-37 25 05.90	28 ± 6	3'7	0.67 ± 0.71	no

^aThe hardness ratio defined as $HR = (H - S)/(H + S)$, where S is the number of counts from 1.0 to 2.5 keV and H is the number of counts from 2.5 to 8 keV.

TABLE 2
RESULTS FROM FITTING VRAYMOND+VPSHOCK+GAUSS MODEL TO THE WHOLE SNR WITH THE 90% CONFIDENCE RANGES.

Parameter	Whole SNR
N_{H} (10^{22} cm ⁻²)	7.1 ^{+0.1} _{-0.1}
Soft component (CIE) ^a	
kT (keV)	0.76 ^{+0.05} _{-0.03}
EM (10^{59} cm ⁻³)	9.9 ^{+1.8} _{-2.3}
Hard component	
kT (keV)	1.44 ^{+0.17} _{-0.13}
$n_e t$ (10^{11} cm ⁻³ s)	4.5 ^{+2.7} _{-1.5}
Si	2.1 ^{+0.2} _{-0.3}
EM (10^{59} cm ⁻³)	2.9 ^{+1.4} _{-0.5}
Gaussian line component	
E (keV)	3.1 (frozen)
dE (keV)	10^{-5} (frozen)
K (phot cm ⁻² s ⁻¹)	$2.9^{+2.3}_{-1.9} \times 10^{-5}$
$\delta\chi^2/\text{dof}$	1.22/339
Unabsorbed X-ray flux (0.5–10 keV)	
F_{total} (ergs cm ⁻² s ⁻¹)	6.5×10^{10}
F_{hard} (ergs cm ⁻² s ⁻¹)	1.7×10^{10}

^acollisional ionization equilibrium

TABLE 3
RESULTS FROM FITTING VRAYMOND OR VPSHOCK MODEL TO SIX SPECTRAL REGIONS IN SNR G349.7+0.2 MARKED IN FIGURE 1 WITH THE 90% CONFIDENCE RANGES.

Parameter	Reg 1	Reg 2	Reg 3	Reg 4	Reg 5	Reg 6
N_{H} (10^{22} cm ⁻²)	6.7 ^{+0.3} _{-0.2}	6.7 ^{+0.3} _{-0.2}	6.5 ^{+0.3} _{-0.3}	7.8 ^{+0.6} _{-0.7}	7.2 ^{+0.3} _{-0.4}	7.8 ^{+0.6} _{-0.4}
kT (keV)	0.92 ^{+0.03} _{-0.07}	0.94 ^{+0.06} _{-0.04}	1.28 ^{+0.08} _{-0.08}	1.28 ^{+0.10} _{-0.07}	1.13 ^{+0.06} _{-0.07}	1.18 ^{+0.08} _{-0.09}
Si	1.4 ^{+0.2} _{-0.3}	1.6 ^{+0.3} _{-0.2}	1.7 ^{+0.3} _{-0.3}	1.6 ^{+0.4} _{-0.2}	1.6 ^{+0.4} _{-0.2}	2.4 ^{+0.6} _{-0.6}
S	1.2 ^{+0.2} _{-0.2}	0.9 ^{+0.2} _{-0.1}	0.8 ^{+0.1} _{-0.1}	1.2 ^{+0.3} _{-0.1}	1.2 ^{+0.2} _{-0.2}	1.5 ^{+0.2} _{-0.3}
$n_e t$ (cm ⁻³ s)	CIE	$1.2^{+1.4}_{-0.5} \times 10^{12}$	$1.1^{+0.9}_{-0.4} \times 10^{12}$	$3.6^{+2.2}_{-1.1} \times 10^{11}$	$8.0^{+5.0}_{-2.9} \times 10^{11}$	$3.8^{+1.9}_{-1.2} \times 10^{11}$
EM (10^{59} cm ⁻³)	1.2 ^{+0.3} _{-0.1}	1.2 ^{+0.2} _{-0.2}	0.6 ^{+0.1} _{-0.06}	0.8 ^{+0.1} _{-0.1}	0.9 ^{+0.1} _{-0.06}	0.9 ^{+0.1} _{-0.1}
$\delta\chi^2/\text{dof}$	1.12/134	1.02/130	1.19/137	1.27/143	0.88/143	0.97/145

TABLE 4
ENERGY RANGES OF NARROW-BAND IMAGES USED FOR DERIVING CONTINUUM-SUBTRACTED AND EQUIVALENT-WIDTH IMAGES IN G349.7+0.2.

Emission Line	Line ev	Left Continuum ev	Right Continuum ev
Si	1750–1950	1550–1700	2100–2250
S	2350–2600	2100–2250	2600–2800

FIG. 1.— [see **f1.jpg**] The 1.0–8.0 keV band ACIS image of G349.7+0.2. Three of five (see Table 1) point sources present in the field around G349.7+0.2 are marked with circles and letters PS. Six regions used for spectral analysis (each with ≈ 5000 counts) are also marked.

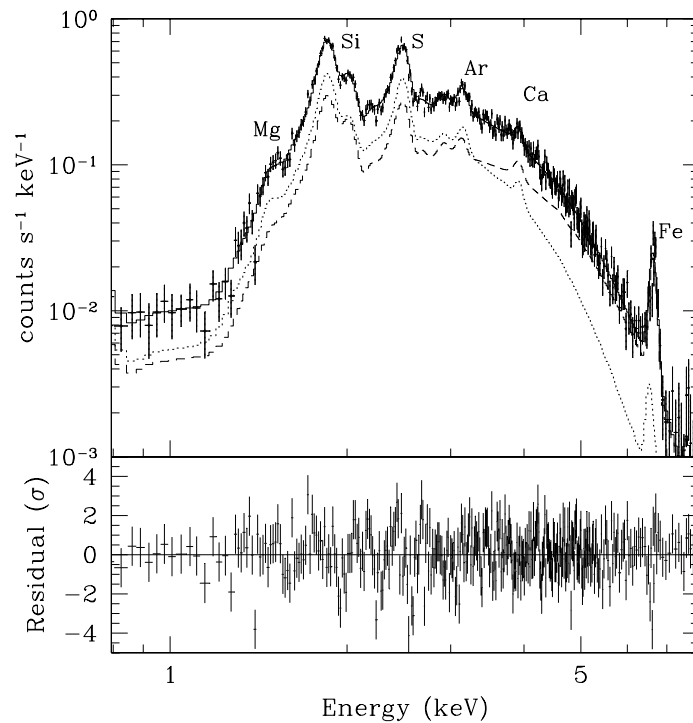


FIG. 2.— ACIS spectrum extracted from the whole SNR, fitted with two-component temperature (VRAYMOND+VPSHOCK+GAUSSIAN) model. The dotted line represents the contribution of the soft component, the dashed line represent the contribution of the hard component, and the solid line is the sum of the both. Residuals from the model are plotted in the lower panel.

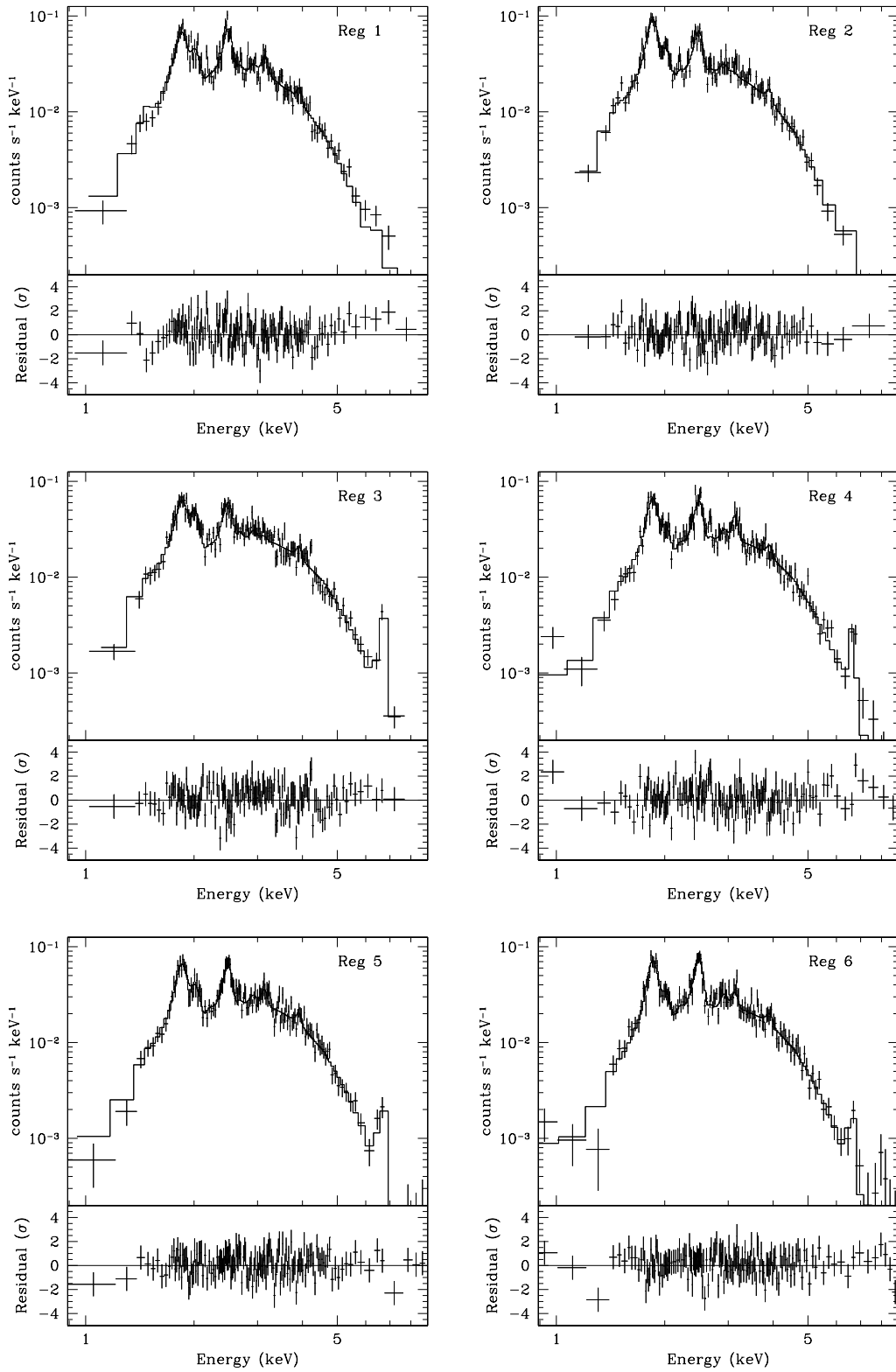


FIG. 3.— ACIS spectra from the six SNR regions marked in Figure 1 and residuals from the best-fit models. Fits parameters are listed in Table 3.

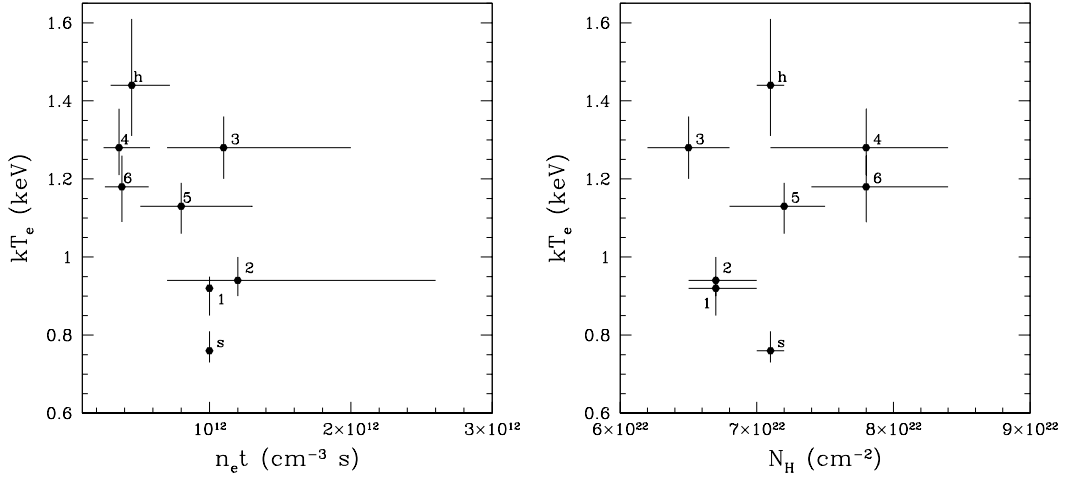


FIG. 4.— The best-fit values and the 90% confidence ranges of different spectral parameters measured in the six SNR regions (marked with numbers) and in the whole SNR (s=soft component, h=hard component). (*Left:*) Temperatures and ionization timescales. (*Right:*) Temperatures and column densities. The plasma temperature in the six spectral regions is intermediate between the temperature measured from the whole SNR, and the eastern-most regions (1 and 2) have the plasma temperature lower than the other regions.

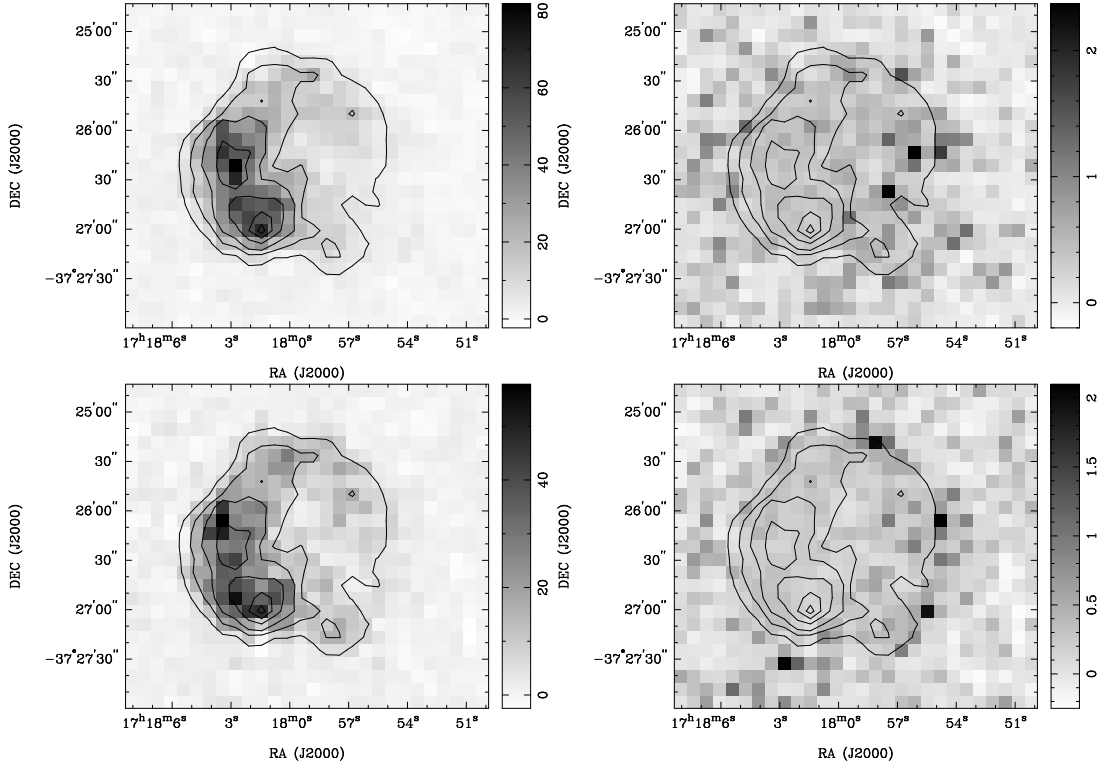


FIG. 5.— CS (*left*) and EW (*right*) images of G349.7+0.2 in Si (*top*) and S (*bottom*) line, binned by 16 pixels (i.e., 1 pixel=8''). Linear scale is in counts pixel⁻¹ for the CS images and in keV for the EW images. The images are overlaid with contours from the 1–8 keV band image binned in the same manner. Contour levels are: 70, 180, 300, 500, 700 and 900 counts arcmin⁻¹.

FIG. 6.— [see **f6.jpg**] The ACIS image overlaid with the Australia Telescope Compact Array 18-cm contours from Lazendic et al. (2004), with resolution of $9' \times 5'$ (P.A. $=-1^\circ$). Greyscale is in counts $\text{arcmin}^{-1} \text{s}^{-1}$. Most of the contour levels (in mJ beam^{-1}) are labeled on the image; the peak two contours are at the 204 and 272 mJ beam^{-1} level. The two images show almost identical morphology.

FIG. 7.— [see **f7a.jpg**, **f7b.jpg**] Molecular line data towards G349.7+0.2 plotted as contours over the ACIS greyscale image. The crosses mark the OH(1720 MHz) maser positions (Frail et al. 1996). (*Top* :) The velocity-integrated (+14 to +20 km s^{-1}) CO 1-0 emission has $60''$ resolution (Reynoso & Mangum 2001). The contour levels are: 4, 9, 20, 29, 35, 40 and 44 K km s^{-1} . (*Bottom* :) The velocity-integrated $2.12 \mu\text{m}$ H_2 1-0 S(1) line emission has the spatial resolution of $\approx 1''$ (Lazendic et al. 2004). The contour levels are: 9, 17 and $35 \times 10^{-5} \text{ erg s}^{-1} \text{ cm}^{-2} \text{ sr}^{-1}$.

FIG. 8.— [see **f8.jpg**] Greyscale image of the velocity-integrated (+14 to +20 km s^{-1}) H I emission towards G349.7+0.2 obtained from the SGPS (e.g., McClure-Griffiths et al. 2001) with $2'.5$ resolution, overlaid with CO integrated over the same velocity range (white contours; Reynoso & Mangum 2001) with $1'$ resolution, and radio continuum (heavy white contours; Lazendic et al. 2004). The compact radio continuum source is an ultra-compact H II region IRAS 17147-3725 (Bronfman, Nyman, & May 1996). Greyscale is in K km s^{-1} . The CO (white) contour levels are 6, 10, 18, 26, 36, 41 and 46 K km s^{-1} . The radio continuum (heavy white) contour levels are 10, 17, 34, 68, 136, 205 and 274 mJy. H I emission shows large scale correlation with CO emission.

This figure "f1.jpg" is available in "jpg" format from:

<http://arxiv.org/ps/astro-ph/0409592v1>

This figure "f6.jpg" is available in "jpg" format from:

<http://arxiv.org/ps/astro-ph/0409592v1>

This figure "f7a.jpg" is available in "jpg" format from:

<http://arxiv.org/ps/astro-ph/0409592v1>

This figure "f7b.jpg" is available in "jpg" format from:

<http://arxiv.org/ps/astro-ph/0409592v1>

This figure "f8.jpg" is available in "jpg" format from:

<http://arxiv.org/ps/astro-ph/0409592v1>